




Evidence of dual Shapiro steps in a Josephson junction array

Received: 18 July 2022

Accepted: 18 January 2023

Published online: 02 March 2023

 Check for updates

 Nicolò Crescini ^{1,3}, Samuel Cailleaux^{1,3}, Wiebke Guichard¹, Cécile Naud¹, Olivier Buisson¹, Kater W. Murch ² & Nicolas Roch ¹ ✉

The modern primary voltage standard is based on the a.c. Josephson effect and the ensuing Shapiro steps, where a microwave tone applied to a Josephson junction yields a constant voltage $hf/2e$ determined by only the microwave frequency f , Planck's constant h and the electron charge e . Duality arguments for current and voltage have long suggested the possibility of dual Shapiro steps—that a Josephson junction device could produce current steps with heights determined only by the applied frequency. Here we embed an ultrasmall Josephson junction in a high impedance array of larger junctions to reveal dual Shapiro steps. For multiple frequencies, we detect that the a.c. response of the circuit is synchronized with the microwave tone at frequency f , and the corresponding emergence of flat steps in the d.c. response with current $2ef$, equal to the transport of a Cooper pair per tone period. This work extends phase–charge duality to Josephson circuits, which opens a broad range of possibilities in the field of circuit quantum electrodynamics and is an important step towards the long-sought closure of the quantum metrology electrical triangle.

In quantum mechanics, uncertainty relations quantify the incompatibility of quantum operators. For a Josephson junction, these operators are the charge Q and the Josephson phase ϕ , which respect $[\phi, Q] = 2ie$, where e is the electron charge^{1,2}. Because of this incompatibility, the suppression of the variance of one of these operators causes the conjugate operator's variance to increase. The balance between phase and charge fluctuations in a junction is determined by the ratio of two energy scales, that is, the Josephson energy $E_J = \hbar I_c/2e$ and the charging energy $E_C = e^2/2C$, where I_c is the critical current of the junction, C is its capacitance and \hbar is the reduced Planck constant¹. In one limit, $E_J/E_C \gg 1$, the variance of ϕ is small, allowing it to be treated as a classical variable, and the dynamics of a junction shunted by a current source is described by a tilted washboard potential $U(\phi)$ (Fig. 1). By applying a microwave tone, the potential is periodically tilted; one fluxon (Φ_0) is transported across the junction at each period, resulting in discrete voltage steps (Shapiro steps) in the I – V (current–voltage characteristics) curve^{3,4}. In contrast, if $E_J/E_C \lesssim 1$, fluctuations in the phase are enhanced, allowing the charge variance to be reduced. In this limit, one expects a

microwave drive to produce dual Shapiro steps^{5–11}; the cyclical tilting of a potential periodic in charge can meter the transport of Cooper pairs across the junction, resulting in current steps proportional to the applied frequency^{12–17}.

An ultrasmall Josephson junction (UJJ) has an E_J/E_C ratio smaller than 1. By treating the phase as an extended variable^{2,18}, which is allowed by the coupling to an environment¹⁹, the junction Hamiltonian reads:

$$H = 4E_C(Q/2e)^2 - E_J \cos(\phi), \quad (1)$$

which, using Bloch's theorem²⁰, can be recast to:

$$H = \sum_s U^{(s)}(q), \quad (2)$$

where we have introduced the quasi-charge q and the Bloch bands $U^{(s)}(q)$ ^{12,13}. Here, q is a continuous variable in units of $2e$ and can be physically interpreted as the displacement charge on the capacitor.

¹Grenoble INP, Institut Néel, Univ. Grenoble Alpes, CNRS, Grenoble, France. ²Department of Physics, Washington University, St. Louis, MO, USA.

³These authors contributed equally: Nicolò Crescini and Samuel Cailleaux. ✉e-mail: nicolas.roch@neel.cnrs.fr

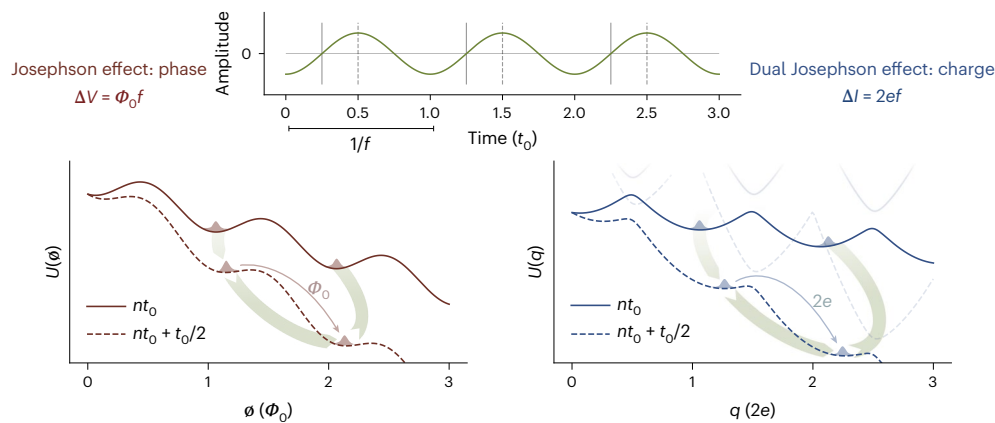


Fig. 1 | The Shapiro steps and their dual. Usual Shapiro steps are realized by periodically tilting the washboard potential of a Josephson junction with $E_J \gg E_C$. Since the phase is a well-defined variable, the driving of the potential yields steps of constant voltage $\Phi_0 f$ (where $\Phi_0 = h/2e$ is the flux quantum) that are precisely determined by the metered transport of fluxons. In contrast, the dual

phenomenon (right side) uses the lowest Bloch band of a junction with $E_J \leq E_C$ (higher bands in the picture are shown only for illustrative purposes). With charge as the well-defined variable, current steps of value $2ef$ determined by the cyclic transport of Cooper pairs appear: the dual Shapiro steps.

As this junction is embedded in an environment of impedance R , thermal and quantum fluctuations can further increase the charge variance^{21,22}. Here, charge fluctuations are bounded by the energy–time uncertainty relation $\Delta E \Delta t > \hbar$, where the charging time of the junction capacitance is $\Delta t = RC$. Hence, large impedance is necessary to reduce the charge fluctuations, in particular to have $\Delta E < E_C$ requires, $R > h/4e^2 \approx 6.45$ k Ω , the quantum of resistance. Additionally, to suppress thermal fluctuations, one has to cool the environment to ultra-cryogenic temperatures $T < E_C/k_B$, where k_B is Boltzman constant. Under these conditions, the charge is localized and can thus be treated as a classical variable. Q is well approximated by q as its dynamics is restricted to the first Bloch band ($s = 0$), thereby realizing the periodic potential $U(Q) \simeq U^{(0)}(q) = E_Q \cos(\pi Q/e)$ –dual to $U(\phi)$ (Fig. 1) The periodic potential corresponds to a non-linear capacitance–dual to the non-linear inductance typically associated with a Josephson junction. Table 1 summarizes the dual transformations in Josephson circuits^{23,24}. Along these lines, the amplitude of the first Bloch band is related to the critical voltage $V_c = \pi E_Q/e$, the minimum voltage required for a flow of d.c. current across the junction. V_c is dual to the critical current, the current below which no voltage is generated⁸. Upon the application of a d.c. current, the system exhibits Bloch oscillations^{12,25}, that is, voltage oscillations arising in the presence of a constant force, a phenomenon dual to the a.c. Josephson effect. If these oscillations are synchronized with an external tone, they yield dual Shapiro steps^{10,12,26}.

Prior work has demonstrated some of the essential components for the exploration of Josephson circuits’ duality. A charge periodic potential has been obtained in UJJs^{25,27–29} or nanowires^{30–33}. Large impedance environments have been realized by using resistors²⁵, suspended³⁴ or low dielectric constant³⁵ substrates, high kinetic inductance materials^{30,33,36,37} or metamaterials^{21,22,38–40}. Despite this progress, a clear demonstration of dual Shapiro steps is still missing. In this work, we harness techniques from circuit quantum electrodynamics⁴¹ to study the interplay of microwave drive and d.c. bias of an UJJ embedded in a superconducting high-impedance environment. Utilizing low noise microwave spectroscopy, we observe the onset of a microwave mode synchronized with an external tone. In turn, we observe current plateaux proportional to the frequency of the microwaves. These two experimental observations are consistent with synchronized Bloch oscillations and dual Shapiro steps.

Figure 2 shows the device used in this work, which we refer to as a Bloch array, consisting of a superconducting quantum interference device (SQUID) formed by two ultrasmall junctions surrounded by two linear JJ superinductances which provide the high impedance

Table 1 | Summary of dual transformations in a Josephson circuit

Dual transformations	
$E_J/E_C \gg 1$	$E_J/E_C \leq 1$
Classical (localized) ϕ	Classical (localized) q
Tilted washboard $U(\phi)$	First Bloch band $U(Q)$
Non-linear inductance	Non-linear capacitance
Critical current I_c	Critical voltage V_c
A.c. Josephson effect	Bloch oscillations
Fluxon transport	Cooper pair transport
Shapiro steps	Dual Shapiro steps

environment. The array consists of Al/AIO_x/Al junctions in a stripline geometry on a fused silica wafer, which reduces the capacitance to ground⁴². The SQUID is formed by junctions with area of $0.2 \times 0.2 \mu\text{m}^2$ ($E_J/E_C \approx 0.4$) each, and the superinductance comprises an array of $N_s/2 = 3,500$ junctions with an area of $1 \mu\text{m}^2$ ($E_J/E_C \approx 250$). The array’s first junctions reported in the figure are slightly larger than the ones in the rest of the device (not shown). This is not expected to result in any difference. From these parameters, we estimate a first Bloch band width of $E_Q/h = 2.5$ GHz and a minimum gap of 7.9 GHz between the first and the second Bloch band. The characteristic impedance and inductance of each superinductance are $Z = 14.8$ k Ω and $L/2 = 6.6$ μH , respectively. A scanning electron microscopy (SEM) image is shown in Fig. 2b. Further details are given in the Methods section. The Bloch array is studied with an experimental setup allowing for simultaneous d.c. and radiofrequency (RF) measurements (Fig. 2c). Measurements are performed at the base temperature of a dilution refrigerator with $T \approx 23$ mK.

We first examine the d.c. and RF response of the Bloch array separately. The I – V curve is obtained by biasing the device with the voltage V_0 and reading out the corresponding current I_0 . Here, we consider $|V_0| \leq 10$ mV, while the whole I – V curve is described in the Methods section. As shown in the plot, the current–voltage characteristics exhibits several current peaks^{43,44} evenly spaced by 2Δ , the superconducting gap of aluminium. These peaks can be understood as follows: When a voltage is applied to the Bloch array, one of the junctions (J_1) is biased to the sub-gap state, behaving as a large series resistance, and the flow of current is suppressed. Consequently, V_0 drops on J_1 until it reaches the gap. When $V_0 = 2\Delta$, J_1 turns normal conducting, and I_0

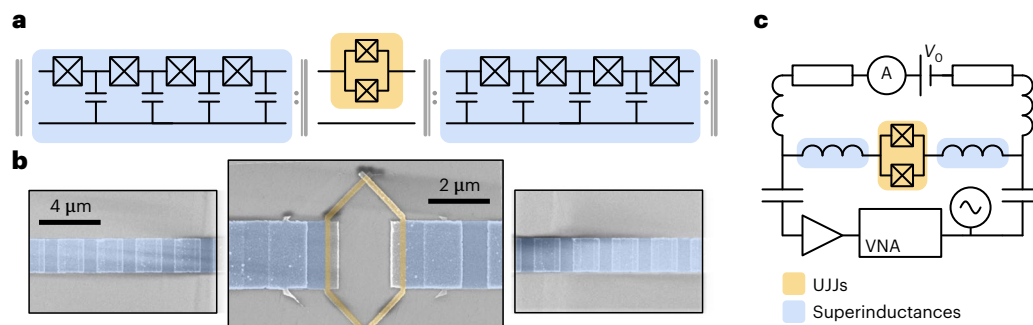


Fig. 2 | Overview of device and measurement setup. **a**, Circuit schematic of the Bloch array. **b**, SEM image of the UJJ and of the beginning of JJ arrays nominally identical to the one under test. **c**, Simplified schematic of the measurement setup

including the device, bias tees, damping resistors, d.c. and RF electronics, and a vector network analyser (VNA). In all the panels (**a**, **b**, **c**), the UJJ is shown in orange and the JJ array in blue. Circled A, amperometer; V_0 is a voltage source.

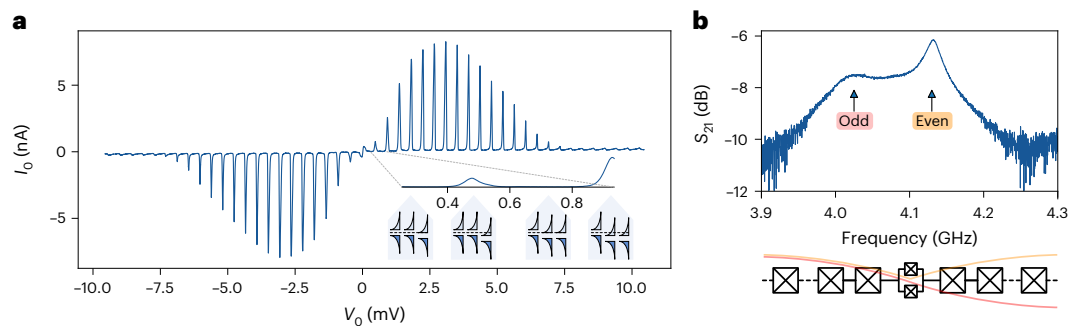


Fig. 3 | D.c. and RF characterization of the Bloch array. **a**, The low voltage I - V curve detailed in the text. Inset: Schematic showing the switching mechanism of the junctions in the array with a band model. The dashed line is a guide to the eye. **b**, The microwave transmission of the Bloch array's fourth mode doublet, with the voltage profile of odd and even modes below.

sharply increases until a second junction J_2 is biased into the sub-gap state, introducing again a large series resistance and suppressing the current. To turn both the junctions resistive, the voltage needs to be 4Δ , and the process repeats. A schematic of this mechanism is shown Fig. 3a (inset). This successive switching resets the voltage drop across the junctions every 2Δ . In this way, the same physics, and in particular the low voltage physics, repeats at voltages modulo 2Δ as one more junction switches to the normal state per step. Resistively and capacitively shunted junction (RCSJ) simulations of a voltage-biased JJ array (Methods) are in agreement with our observations.

The microwave transmission of a Bloch array exhibits mode doublets, one with odd and one with even symmetry²² (Fig. 3b). The odd mode is coupled to the UJJ at the centre of the array, while the even one is not, as comprehensively discussed by Leger et al.²². The frequency of the odd mode is lower than that of the even mode, which is consistent with the presence of a capacitive element between the left and right superinductances. This agrees with duality considerations, according to which the UJJ should behave as a non-linear capacitance. Leveraging the d.c. and microwave capabilities of our setup, we investigate the effect of an applied voltage on the modes of the Bloch array. By measuring the transmission coefficient S_{21} as a function of V_0 , we observe that, between two current peaks, the doublet is visible yet starts to degrade when current flows through the array. The mode doublet is replicated after every 2Δ switch, compatible with the mechanism depicted by the I - V curve. The full measurement is detailed in the Methods section and in Extended Data Fig. 5.

We now study the behaviour of the Bloch array in the presence of an additional applied microwave tone. Figure 4a shows the microwave transmission of the Bloch array near the mode doublet at 4.1 GHz for different frequencies f of the microwave tone with power $p = -5.0$ dBm. We observe that the array odd mode is influenced by the microwave

tone and drifts away from f , in a mode repulsion fashion. A mode synchronous with the pump appears when the frequency exceeds approximately 4.02 GHz and fades around $f \approx 4.11$ GHz. This behaviour is further studied by varying p at $f = 4.04$ GHz (Fig. 4b). At low power, the array is essentially unaltered by the tone, until p reaches -20 dBm and the spectrum shows a profile corresponding to a Fano resonance, whose maximum-to-minimum separation increases with p . The most noteworthy feature is at $p \approx -5$ dBm (Fig. 4c). We clearly observe a microwave mode with a Lorentzian shape and linewidth of about 1 MHz, centred at f , which disappears at higher p . We refer to this feature as a Bloch mode, as it is consistent with Bloch oscillations synchronized with the external tone⁴⁵.

Focusing on this microwave synchronized Bloch mode ($f = 4.04$ GHz, $p = -5.0$ dBm), we now examine the I - V characteristic of the Bloch array under microwave irradiation (Fig. 4d). The I - V characteristic presents a wide central region with no current or supercurrent peaks. Outside this central part, we observe that, for both positive and negative voltage, current plateaux form before the 2Δ current peaks. The current corresponding to their flatter part is $2ef$ within a 0.1% accuracy. These observations are supported by simulations (Methods) showing that the steps should emerge as a flat current region immediately before the upward slope of the 2Δ peaks.

Figure 5 displays a more detailed investigation of these current steps. Figure 5a shows the heights of three different current plateaux versus p , which have a saturation point at $p = -5$ dBm and $I_0 = 2ef$. The tone power p influences the height of the step, and the flatter quantized steps are obtained only for a given power range, in a fashion very similar to what is observed for standard Shapiro steps⁴⁶. To further assess the stability of the step, we modulate the microwave power p and measure the corresponding I_0 variation with a lock-in amplifier. The result is displayed in Fig. 5b and shows that dI_0/dp falls to the noise

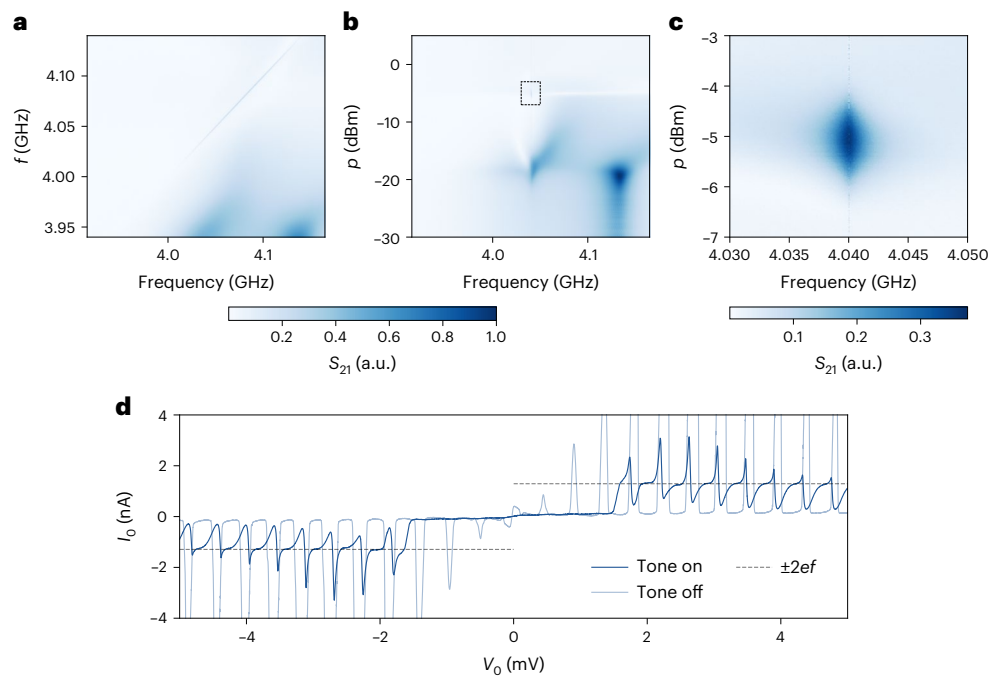


Fig. 4 | Emergence of Bloch oscillations and dual Shapiro steps. **a**, The frequency of the external tone f is changed to observe its effect on the transmission spectrum of the Bloch array. **b**, A similar measurement where we vary the power p of the tone at fixed frequency $f = 4.04$ GHz. **c**, The transition

between tone interference and microwave mode is clearly visible in this plot showing the dashed rectangle in **b**. **d**, The I - V characteristics measured for $f = 4.04$ GHz and $p = -5.0$ dBm. Between two current peaks, the plateaux current is $\pm 2ef$ (dashed grey lines).

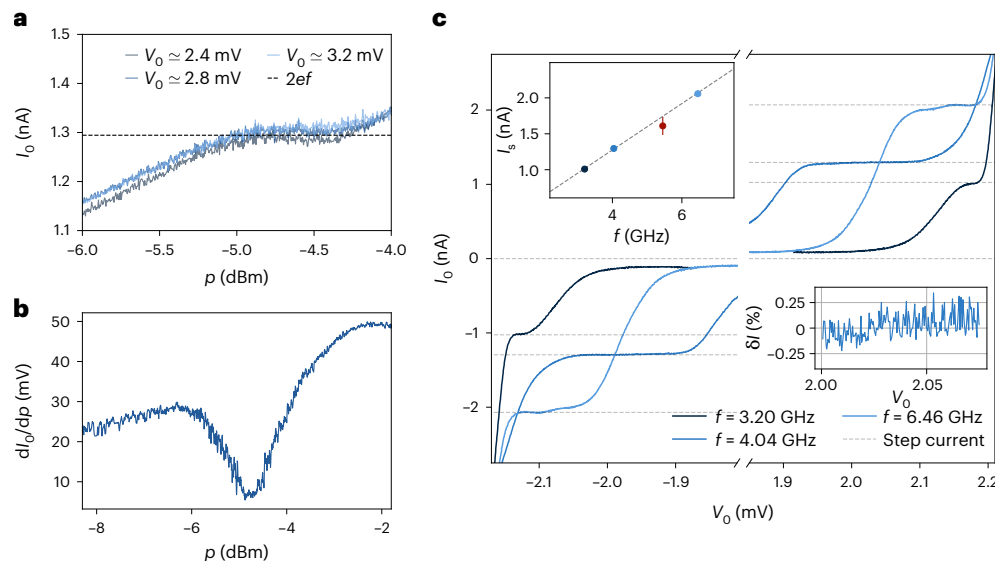


Fig. 5 | Current plateaux at different microwave tone frequency and power. **a**, The average plateaux current at different microwave powers p for three voltages. **b**, Lock-in measurement collected by modulating the microwave power p and detecting the corresponding current variation at $V_0 = 2.4$ mV. **c**, For three different values of f , we follow the procedure described in the text to observe

current plateaux whose amplitude correspond to the one of the first dual Shapiro step (dashed grey line). Inset: The relation between the step current I_s and the tone frequency. The fitted slope is consistent with $2e$. The red point's I - V curve is omitted for clarity (see Methods section for further details).

floor at $p \approx -5$ dBm, suggesting a current that is independent of the microwave power. The noise floor is estimated by performing the same measurement at a much higher power, which completely suppresses the peaks. The emergence of the Bloch mode, the current saturation and the minimum of the dI_0/dp curve happen in the same power range, suggesting that this is the quantum-locking range of our device.

Microwave power is delivered to the UJJ when the tone is on resonance with the odd microwave mode of the array. Utilizing microwave

spectroscopy, we identify other suitable working points (Methods), corresponding to different mode doublets of the Bloch array. Figure 5c shows the lowest bias voltage current step common to three additional frequencies. The parameters and additional measurements used to obtain these curves are detailed in the Methods section, and in particular in Extended Data Fig. 6. For a total of four mode frequencies, we observe that I_0 flattens at the corresponding $2ef$ for $f = 3.20$, 4.04, 5.45 and 6.46 GHz. Finally, Fig. 5c (inset) shows the frequency

dependence of I_s , the average current on the flat part of each step. Through the slope of the fitting line, we can estimate a Cooper pair's charge of $(3.23 \pm 0.07) \times 10^{-19}$ C. Even though the measurement was not optimized, the average deviation from the expected current $\delta I = I_0/2ef - 1$ on the 4 GHz step is $\langle \delta I^2 \rangle^{1/2} \leq 0.001$, limited by the setup noise in an averaging time of 1 min (Fig. 5c, inset). Steps of higher current are desirable for metrological applications. This could be achieved by increasing E_J and E_C proportionally. A larger E_J would provide a higher critical current of the UJJ while keeping a negligible Landau–Zener transition rate. Then, E_C must also be increased to keep $E_J/E_C \approx 1$ and a proper charge dynamics.

The environment of the UJJ, formed by the Josephson junction arrays, does more than provide the high impedance required for charge localization. As discussed above, the switching of the junctions in the array absorbs the majority of the applied voltage, allowing the UJJ to remain in the superconducting state even at high V_0 . Furthermore, the microwave response of the device allows us to selectively apply a microwave drive to the UJJ, causing the formation of the Bloch mode and the corresponding onset of current steps. In contrast, no effect is observed when driving the even mode that does not couple to the UJJ.

We also compare briefly with the work of Shaikhaidarov et al., where quantized current steps in a superconducting nanowires system were observed. With respect to Josephson junctions, nanowires show a higher working frequency and a wider dynamic power range⁴⁷. On the other hand, the steps achieved in this work are substantially flatter, and a JJ device can be thoroughly characterized and, in principle, entirely described by a microscopic model. The evidence of this effect in two different platforms further strengthens the underlying theory.

In the quantum metrology electrical triangle, voltage and frequency can be related via the a.c. Josephson effect, while current and voltage via the quantum Hall effect. Here, we study the third edge of the triangle by relating current and frequency via the charge $2e$ of a Cooper pair, the last coherent effect needed to close the triangle. Our work highlights how the Bloch array can be harnessed to engineer dissipation, thereby resolving charge at the expense of phase fluctuations, a regime dual to what is commonly achieved in Josephson circuits (localized phase and large charge fluctuations). We take advantage of this new configuration and observe quantized current steps, that is, dual Shapiro steps. This first step in this direction indicates that the rich physics of the Bloch array will have to be fully mastered in the process of developing the dual Josephson effect into a metrological definition of the ampere^{16,48}. This also opens exciting opportunities from the perspective of fundamental physics via tests of quantum electrodynamics through the closure of the triangle⁴⁹ or further exploration of phase–charge duality in Josephson devices.

Online content

Any methods, additional references, Nature Portfolio reporting summaries, source data, extended data, supplementary information, acknowledgements, peer review information; details of author contributions and competing interests; and statements of data and code availability are available at <https://doi.org/10.1038/s41567-023-01961-4>.

References

- Tinkham, M. *Introduction to Superconductivity*, 2nd edn (Dover, 2004).
- Sonin, E. B. Quantum rotator and Josephson junction: compact vs. extended phase and dissipative quantum phase transition. *Low Temperature Physics* **48**, 400 (2022); <https://doi.org/10.1063/10.0010205>
- Josephson, B. D. Possible new effects in superconductive tunnelling. *Phys. Lett.* **1**, 251–253 (1962).
- Shapiro, S. Josephson currents in superconducting tunneling: the effect of microwaves and other observations. *Phys. Rev. Lett.* **11**, 80–82 (1963).
- Schön, G. & Zaikin, A. D. Quantum coherent effects, phase transitions, and the dissipative dynamics of ultra small tunnel junctions. *Phys. Rep.* **198**, 237–412 (1990).
- Spiller, T. P., Clark, T. D., Prance, R. J., Prance, H. & Poulton, D. A. Electromagnetic duality in quantum circuits. *Il Nuovo Cim. B Ser. 11* **105**, 43–52 (1990).
- Ingold, G.-L. & Nazarov, Y. V. In *Single Charge Tunneling: Coulomb Blockade Phenomena In Nanostructures* (eds Grabert, H & Devoret, M. H.) pp 21–107 (Springer, 1992).
- Corlevi, S., Guichard, W., Hekking, F. W. J. & Haviland, D. B. Phase-charge duality of a Josephson junction in a fluctuating electromagnetic environment. *Phys. Rev. Lett.* **97**, 096802 (2006).
- Arutyunov, K. Y., Golubev, D. S. & Zaikin, A. D. Superconductivity in one dimension. *Phys. Rep.* **464**, 1–70 (2008).
- Guichard, W. & Hekking, F. W. J. Phase–charge duality in Josephson junction circuits: role of inertia and effect of microwave irradiation. *Phys. Rev. B* **81**, 064508 (2010).
- Kerman, A. J. Flux–charge duality and topological quantum phase fluctuations in quasi-one-dimensional superconductors. *N. J. Phys.* **15**, 105017 (2013).
- Likharev, K. K. & Zorin, A. B. Theory of the Bloch-wave oscillations in small Josephson junctions. *J. Low. Temp. Phys.* **59**, 347–382 (1985).
- Averin, D. V., Zorin, A. B. & Likharev, K. K. Bloch oscillations in small Josephson junctions. *Sov. Phys. JETP* **61**, 7 (1985).
- Averin, D. V. & Odintsov, A. A. Phase locking of the Bloch oscillations in ultrasmall Josephson junctions. *Phys. B* **165–166**, 935–936 (1990). LT-19.
- Hu, G. Y. & O'Connell, R. F. Bloch oscillations in small-capacitance Josephson junctions. *Phys. Rev. B* **47**, 8823–8830 (1993).
- Pekola, J. P. et al. Single-electron current sources: toward a refined definition of the ampere. *Rev. Mod. Phys.* **85**, 1421–1472 (2013).
- Bylander, J., Duty, T. & Delsing, P. Current measurement by real-time counting of single electrons. *Nature* **434**, 361–364 (2005).
- Carruthers, P. & Nieto, M. M. Phase and angle variables in quantum mechanics. *Rev. Mod. Phys.* **40**, 411–440 (1968).
- Loss, D. & Mullen, K. Effect of dissipation on phase periodicity and the quantum dynamics of Josephson junctions. *Phys. Rev. A* **43**, 2129–2138 (1991).
- Ashcroft, N. W. & Mermin, N. D. *Solid State Physics* (Holt, Rinehart, and Winston, 1976).
- Puertas Martínez, J. et al. A tunable Josephson platform to explore many-body quantum optics in circuit-QED. *npj Quantum Inf.* **5**, 19 (2019).
- Léger, S. ébastien et al. Observation of quantum many-body effects due to zero point fluctuations in superconducting circuits. *Nat. Commun.* **10**, 5259 (2019).
- Shahar, D., Tsui, D. C., Shayegan, M., Shimshoni, E. & Sondhi, S. L. Evidence for charge–flux duality near the quantum Hall liquid-to-insulator transition. *Science* **274**, 589–592 (1996).
- Ovadia, M., Kalok, D., Sacépé, B. & Shahar, D. Duality symmetry and its breakdown in the vicinity of the superconductor–insulator transition. *Nat. Phys.* **9**, 415–418 (2013).
- Kuzmin, L. & Haviland, D. Observation of the Bloch oscillations in an ultrasmall Josephson junction. *Phys. Rev. Lett.* **67**, 2890–2893 (1991).
- Di Marco, A., Hekking, F. W. J. & Rastelli, G. Quantum phase-slip junction under microwave irradiation. *Phys. Rev. B* **91**, 184512 (2015).
- Andersson, K., Delsing, P. & Haviland, D. Synchronous Cooper pair tunneling in a 1D-array of Josephson junctions. *Phys. B* **284–288**, 1816–1817 (2000).
- Weiβl, T. et al. Bloch band dynamics of a Josephson junction in an inductive environment. *Phys. Rev. B* **91**, 014507 (2015).

29. Cedergren, K. et al. Insulating Josephson junction chains as pinned Luttinger liquids. *Phys. Rev. Lett.* **119**, 167701 (2017).
30. Lau, C. N., Markovic, N., Bockrath, M., Bezryadin, A. & Tinkham, M. Quantum phase slips in superconducting nanowires. *Phys. Rev. Lett.* **87**, 217003 (2001).
31. Lehtinen, J. S., Zakharov, K. & Arutyunov, K. Y. Coulomb blockade and Bloch oscillations in superconducting Ti nanowires. *Phys. Rev. Lett.* **109**, 187001 (2012).
32. Wang, Z. M., Lehtinen, J. S. & Arutyunov, K. Y. Towards quantum phase slip based standard of electric current. *Appl. Phys. Lett.* **114**, 242601 (2019).
33. Webster, C. H. et al. NbSi nanowire quantum phase-slip circuits: dc supercurrent blockade, microwave measurements, and thermal analysis. *Phys. Rev. B* **87**, 144510 (2013).
34. Peruzzo, M. et al. Geometric superinductance qubits: controlling phase delocalization across a single Josephson junction. *PRX Quantum* **2**, 040341 (2021).
35. Rolland, C. et al. Antibunched photons emitted by a dc-biased Josephson junction. *Phys. Rev. Lett.* **122**, 186804 (2019).
36. Yoshihiro, K. Observation of “Bloch oscillations” in granular tin films. *Phys. B* **152**, 207–211 (1988).
37. Grünhaupt, L. et al. Granular aluminium as a superconducting material for high-impedance quantum circuits. *Nat. Mater.* **18**, 816–819 (2019).
38. Bell, M., Sadovskyy, I., Ioffe, L., Kitaev, A. & Gershenson, M. Quantum superinductor with tunable nonlinearity. *Phys. Rev. Lett.* **109**, 137003 (2012).
39. Masluk, N., Pop, I., Kamal, A., Mineev, Z. & Devoret, M. Microwave characterization of Josephson junction arrays: implementing a low loss superinductance. *Phys. Rev. Lett.* **109**, 137002 (2012).
40. Pechenezhskiy, I. V., Mencia, R. A., Nguyen, L. B., Lin, Yen-Hsiang & Manucharyan, V. E. The superconducting quasicharge qubit. *Nature* **585**, 368–371 (2020).
41. Blais, A., Grimsmo, A. L., Girvin, S. M. & Wallraff, A. Circuit quantum electrodynamics. *Rev. Mod. Phys.* **93**, 025005 (2021).
42. Arndt, L., Roy, A. & Hassler, F. Dual Shapiro steps of a phase-slip junction in the presence of a parasitic capacitance. *Phys. Rev. B* **98**, 014525 (2018).
43. Haviland, D. B., Andersson, K. & Ågren, P. Superconducting and insulating behavior in one-dimensional Josephson junction arrays. *J. Low. Temp. Phys.* **118**, 733–749 (2000).
44. Dolata, R., Scherer, H., Zorin, A. B. & Niemeyer, J. Single-charge devices with ultrasmall Nb/AlO_x/Nb trilayer Josephson junctions. *J. Appl. Phys.* **97**, 054501 (2005).
45. Lenz, G., Talanina, I. & de Sterke, C. M. Bloch oscillations in an array of curved optical waveguides. *Phys. Rev. Lett.* **83**, 963–966 (1999).
46. Levinsen, M. T., Chiao, R. Y., Feldman, M. J. & Tucker, B. A. An inverse ac Josephson effect voltage standard. *Appl. Phys. Lett.* **31**, 776–778 (1977).
47. Shaikhaidarov, R. S. et al. Quantized current steps due to the a.c. coherent quantum phase-slip effect. *Nature* **608**, 45–49 (2022).
48. Göbel, E. O. & Siegner, U. *The New International System of Units (SI) – Quantum Metrology and Quantum Standards* (Wiley, 2019).
49. Sailer, T. et al. Measurement of the bound-electron *g*-factor difference in coupled ions. *Nature* **606**, 479–483 (2022).

Publisher's note Springer Nature remains neutral with regard to jurisdictional claims in published maps and institutional affiliations.

Springer Nature or its licensor (e.g. a society or other partner) holds exclusive rights to this article under a publishing agreement with the author(s) or other rightsholder(s); author self-archiving of the accepted manuscript version of this article is solely governed by the terms of such publishing agreement and applicable law.

© The Author(s), under exclusive licence to Springer Nature Limited 2023

Methods

This section is organized as follows. In the first two sections, we describe the phase–charge duality and a semiclassical model that can give intuition into the observations, and simulation results from a minimal RCSJ model. In the third section, we detail the device fabrication, parameters and experimental measurement setup. The fourth section presents the full I – V curve of the device as well as its flux dependence, while the fifth one describes the microwave properties of the device. The last two sections display the characterization of the microwave modes used for the observation of the current steps and their power and flux dependence.

Semiclassical model and exact duality

The two energy scales in a Josephson junction are the Josephson energy E_J and the charging energy E_C . A large E_J/E_C ratio is used, for example, for the Josephson voltage standard⁵⁰ or in transmon qubits^{51,52}, where an almost classical behaviour of the superconducting phase is favourable. When $E_J \lesssim E_C$, the charge of a single electron is relevant and quantum phase fluctuations are not negligible. In this regime, charge dynamics can be dual to the Josephson phase dynamics, provided that the environmental impedance and inductance L are large^{10,26,41}. Equation (1) describes a particle in a one-dimensional lattice, whose spectrum consists of Bloch bands²⁰ (Fig. 1). If the dynamics is restricted to the first Bloch band, and the bath response is ohmic with resistance R (ref. 10), the equation of motion for the charge is given by:

$$L\ddot{Q} + R\dot{Q} + V_c \sin\left(\frac{\pi}{e}Q\right) = V_0 + V_1, \quad (3)$$

where V_c is the critical voltage of the junction, V_0 and V_1 are the d.c. and a.c. applied voltages, respectively, and the shape of the first Bloch band is approximated as $\sin(\pi Q/e)$. Equation (3) is the exact dual to the equation of motion of a large E_J/E_C ratio JJ. While equation (3) does not accurately model the complex physics of the Bloch array, it does provide useful intuition and serves as a guide for choosing the system parameters.

Following the work of Guichard and Hekking¹⁰, we calculate the time evolution of the system for a fixed voltage, allowing us to produce the I – V characteristic of the circuit (Extended Data Fig. 1). The capacitively shunted junction in series with a resistance and an inductance system under consideration is reported in the lumped element schematic in Extended Data Fig. 1 (inset). The usual phase dynamics associated with the Josephson tunnelling is replaced by its dual counterpart: the quasi-charge dynamics. In this way, instead of the voltage Shapiro steps, one can expect quantized current steps. As with prior work¹⁰, here the signal is perturbed with the voltage noise of the resistor and of the readout amplifier. The circuit parameters are the same as the ones in the main text.

RCSJ toy model

The I – V curve of the array is simulated by numerically solving the equations of motion of a chain of N junctions in series with a non-linear capacitor, an inductance and a damping resistor under a voltage drive. Each junction is modelled using the RCSJ model. The total current I_{tot} through a junction is thus the sum of a capacitive current I_C , a resistive current I_R and a Josephson current I_J :

$$\begin{aligned} I_{\text{tot}} &= I_C + I_R + I_J, \\ I_C &= C\ddot{\phi}_i, \\ I_R &= s(\dot{\phi}_i) \frac{1}{R_N} \dot{\phi}_i, \\ I_J &= (1 - s(\dot{\phi}_i)) I_c \sin\left(\frac{\phi_i}{\phi_0}\right). \end{aligned} \quad (4)$$

where ϕ_i is the superconducting phase drop across the i th junction, R_N is its normal state resistance, C is its capacitance and I_c is its critical

current. We model the gap transition of the junction through the factor $s(\dot{\phi}_i)$, which goes smoothly from 0 when $|\dot{\phi}_i| < 2\Delta$ to 1 when $|\dot{\phi}_i| > 2\Delta$. The factor then smoothly turns off the Josephson element and turns on the resistance. We found that the exact shape of the function s does not impact the resulting I – V characteristics as long as the transition is sharp. All the results presented used a scaled sigmoid for the transition function. The charge and its associated current $I_{\text{tot}} = \dot{Q}$ are related to the bias voltage V by an equation similar to equation (3):

$$V = L\ddot{Q} + R\dot{Q} + V_c \sin\left(\frac{\pi}{e}Q\right) + \sum_i \dot{\phi}_i. \quad (5)$$

We then solve equations (4) and (5) using a Runge–Kutta method of order four with a time step of $dt = 0.02 RC$. We then average the current $\langle I_{\text{tot}} \rangle$ to obtain its d.c. component and plot the I – V characteristic.

Due to the complexity of simulating the response of $N_a = 3,500$ JJs, we focus on a system with $N = 4$ junctions embedded in a circuit with inductance $L = 5 \mu\text{H}$, which captures the inductance of the remaining JJs that form the superinductance. Additionally, we slightly vary the critical current of each junction so as to mimic fabrication variability. This in turn fixes the order in which the junctions become resistive: the one with the lowest I_c switches first, then the second lowest and so on. We fix the initial conditions of the simulation to be $(0, 0)$ for each degree of freedom at $t = 0$ and then ramp up the voltage from 0 to V on a timescale of approximately $10^5 dt$.

Extended Data Fig. 2 displays the I – V characteristic for the chosen parameters, with and without an applied microwave tone. Many features that we observe in the experimental I – V curve are qualitatively reproduced by the simulation. First, we observe current peaks, spaced by 2Δ , corresponding to the successive switching of junctions in the array. Second, when the microwave tone is applied, we observe the formation of current plateaux just before the voltages at which the current peaks occur. These current plateaux are repeated for each current peak.

Other features of this simple simulation do not qualitatively match the experimental I – V curves. Whereas the height of the simulated current peaks is of order I_c and monotonically decreasing with voltage, the experimental current peaks are all well below the estimated I_c , with heights suppressed for small V_0 . This qualitative difference points to aspects of the UJJ, which is simplified in the model. Moreover, it should be emphasized that our current simulations are also simplified in terms of noise, ground capacitance and the number of junctions simulated.

Device and experimental setup

The device consists of Al/AlO_x/Al junctions in a micro-stripline geometry, fabricated by using the shadow evaporation technique and electron beam lithography on a fused silica wafer. The substrate choice is related to the minimization of ground capacitances, which, being proportional to the dielectric constant, are reduced by about four fold with respect to silicon. Reduced ground capacitance and large inductance produce a high impedance and prevent Landau–Zener transitions between Bloch bands, which might suppress the amplitude of Bloch oscillations⁴². Details on the fabrication procedure can be found in the data repository of this work³³.

The superinductance is formed from JJs with capacitance $C_a \approx 50$ fF estimated from their area by using the expected capacitance per unit area of $\sigma_c = 45$ fF μm^{-2} . Each UJJ has an area of $0.04 \mu\text{m}^2$, from which we can similarly estimate a capacitance of $C = 1.8$ fF.

A detailed schematic of the setup used in this work is reported in Extended Data Fig. 3. The experimental apparatus can simultaneously perform d.c. and RF measurements (Fig. 2c). This is achieved using two off-chip bias-tees that decouple kilohertz frequency measurements from the ones in the gigahertz range. The two ports of the Bloch array are connected to the bias-tees via 50Ω -matched lines. At the lowest temperature stage, the d.c. lines feature 45 MHz π -filters, 50Ω damping

resistors in series and Eccosorb filters. Further RC and π -filters are applied at room temperature, being the main source of damping in the circuit. The current I_0 is amplified with a low noise transimpedance amplifier, while the readout and voltage bias are performed with a real-time analogue-to-digital converter (Adwin-Gold II).

The I - V curves are collected by biasing the device with triangular voltage ramps with period ranging from 10 ms to 10 s, depending on the measurement conditions and voltage range. To apply a magnetic field on the sample, we employ a superconducting coil anchored to the sample holder. The periodicity measured in the I - V response agrees with that estimated by considering the SQUID area and the magnetic field produced by the coil. Microwaves are applied to the sample via a high frequency line with an attenuation of about 60 dB, which is connected to one of the bias-tees, while spectroscopic measurements are performed with extra 30 dB of attenuation. The second bias-tee's high frequency port is connected to an isolator and then to a high electron mobility transistor amplifier working in the 4–8 GHz frequency range and with a noise temperature of about 5 K. Further amplification is performed at room temperature, before reading out the signal by using a vector network analyser. The setup is housed in an inverted dilution refrigerator with a base temperature of 23 mK.

Full I - V curve and flux dependence

The current–voltage characteristics of the Bloch array are reported in Extended Data Fig. 4. Extended Data Fig. 4a shows the I - V curves over the largest voltage span, which approaches the resistive branch of the whole array at $2N_a\Delta \approx \pm 3.2$ V. At applied voltages below the gap transition, the I - V characteristic has two resistive branches and a central plateau of about $\Delta_s \approx 1$ V, where its resistance is larger than 100 M Ω (Extended Data Fig. 4b). This is in agreement with prior measurements and theory³⁴, and we notice that the behaviour of this part of the I - V curve is reminiscent of a Coulomb staircase⁷. At a lower voltage scale (Fig. 3a and Extended Data Fig. 4c), more features appear^{43,44}, whose explanation is reported in the main text. Current peaks are present when the voltage is an integer multiple of 2Δ , and their spacing is understood in terms of a sub-gap to a resistive switching mechanism.

Extended Data Fig. 4d displays the I - V curve for the finest voltage scale. For $V_0 < \Delta$, we detect a low-voltage-current with non-trivial shape, which we associate with a combination of supercurrent and inelastic Cooper pair tunnelling^{7,56,57}. Small applied magnetic fields are expected to tune the E_j/E_C ratio of the UJJ, while the superinductances, being formed of single junctions, are to first order not affected. Extended Data Fig. 4e shows the flux dependence of the low voltage I - V curve of the Bloch array, where at $\pm\pi$ flux we observe suppression of the low-voltage-current^{55,56}.

Microwave measurements of the Bloch array

Microwave spectroscopy is used to measure the resonances of the Bloch array²¹. In particular, we identify several peak doublets, which can be further studied by using two-tone measurements⁵⁶. We probe the transmission of the array near one of the observed resonances at 4.13 GHz and sweep the power and frequency of an additional applied tone. When the tone is resonant with an additional mode of the array, the transmission at the probe mode is affected. From these data, we observe a free spectral range of about 1 GHz between two peaks doublets, and a JJ plasma frequency of 16 GHz, beyond which no modes are observed. From these measurements, we obtain the JJ inductance $L_a \approx 1.9$ nH, capacitance $C_a \approx 50$ fF and ground capacitance $C_g \approx 1.7 \times 10^{-4} C_a = 8.7$ aF. These results are in agreement with the ones obtained by measuring the dispersion relation of a JJ array resonator fabricated in the same batch.

We then extract the two superinductance's impedance and inductance $\sqrt{L_a/C_g} = 14.8$ k Ω and $N_a L_a/2 = 6.6$ μ H, the critical current of the large JJs, $I_c = \hbar/2eL_a \approx 173$ nA, and the one of the UJJs, 12 nA. The spectroscopic data also give information on the UJJs capacitance. Referring

to Fig. 3c, the observed mode splitting yields a capacitance of about $1\text{fF} \approx C/2$, in agreement with the value estimated through the ultrasmall junction's area.

The effect of V_0 on the S_{21} of this mode doublet is displayed in Extended Data Fig. 5. Here, we see how a current flowing in the Bloch array degrades the microwave response of both modes, reducing the transmission. The microwave mode doublet is recovered when I_0 is close to zero, further confirming the interpretation of the I - V curve reported in the main text.

Microwave modes used for observing current steps

To observe the steps at different frequencies of the microwave tone, we identified the suitable peak doublets and their response to the microwave tone using the method displayed in Fig. 4b. The corresponding power dependence for the other observed steps are displayed in Extended Data Fig. 6. In each case, the characteristic shape of the power response guides the choice of p to observe the steps, as it is verified to always be analogue to the one in Fig. 4b.

Referring to Fig. 5c, we note that the 5 GHz step is not displayed since the corresponding I - V curve suffers from a much higher noise with respect to the other three. Repeated measurements show that, with this tone frequency, the Bloch array experiences significant $1/f$ noise that, shifting the position of the peaks during the measurement, compromises the averaging reliability. For this reason, the averaging performed on this curve is extremely limited, leading to a higher current noise, as can be seen from the error bar in Fig. 5c (inset).

Data availability

Raw data, analysis scripts and additional measurements and details are publicly available on Zenodo at <https://zenodo.org/record/6913393>.

Code availability

Raw data, analysis scripts and additional measurements and details are publicly available on Zenodo at <https://zenodo.org/record/6913393>.

References

- Hamilton, C. A. Josephson voltage standards. *Rev. Sci. Instrum.* **71**, 3611–3623 (2000).
- Koch, J. et al. Charge-insensitive qubit design derived from the Cooper pair box. *Phys. Rev. A* **76**, 042319 (2007).
- Schreier, J. A. et al. Suppressing charge noise decoherence in superconducting charge qubits. *Phys. Rev. B* **77**, 180502 (2008).
- Crescini, N., Cailleaux, S., Guichard, W., Naud, C., Buisson, O., Murch, K. & Roch, N. Evidence of dual Shapiro steps in a Josephson junctions array. *Zenodo* <https://doi.org/10.5281/zenodo.6913393> (2022).
- Ergül, A. et al. Phase sticking in one-dimensional Josephson junction chains. *Phys. Rev. B* **88**, 104501 (2013).
- Leppäkangas, J. et al. Antibunched photons from inelastic Cooper-pair tunneling. *Phys. Rev. Lett.* **115**, 027004 (2015).
- Hofheinz, M. et al. Bright side of the Coulomb blockade. *Phys. Rev. Lett.* **106**, 217005 (2011).
- Krupko, Y. et al. Kerr nonlinearity in a superconducting Josephson metamaterial. *Phys. Rev. B* **98**, 094516 (2018).

Acknowledgements

The help of D. Basko is deeply acknowledged and appreciated. The support of the superconducting circuits team of Institut Néel is warmly acknowledged. We are also grateful to J. Aumentado, M. Devoret, T. Duty, S. Florens, D. Haviland, J. Renard, B. Sacepe and I. Snyman for their fruitful discussion and comments on our work. Furthermore, our gratitude goes to the members of the Triangle consortium, namely, P. Joyez, Ç. Girit, C. Ciuti, H. Le Sueur and A. Wagner, for their valuable discussion and insights. The samples were fabricated in the clean room facility of Institut Néel, Grenoble; we would like to thank all the

staff for help with device fabrication. We would like to acknowledge E. Eyraud for his help in the installation of the experimental setup. This work was supported by the French National Research Agency (ANR) in the framework of the TRIANGLE project (ANR-20-CE47-0011). N.C. is supported by the European Union's Horizon 2020 research and innovation programme under Marie Skłodowska-Curie grant agreement QMET no. 101029189. K.W.M. acknowledges support from NSF grant no. PHY-1752844 (CAREER), AFOSR MURI grant no. FA9550-21-1-0202 and ONR grant no. N00014-21-1-2630.

Author contributions

N.C., S.C. and N.R. designed the device and the experiment. N.C. fabricated the samples. N.C. and S.C. set up the experimental apparatus and performed the measurements. N.C. analysed the data. S.C. ran the numerical simulations and fabricated the control samples. All the authors discussed and interpreted the data and the results. N.C. and K.M. drafted the manuscript, which was discussed and improved by S.C. and N.R., before being proof-read and commented on by all authors.

Competing interests

The authors declare no competing interests.

Additional information

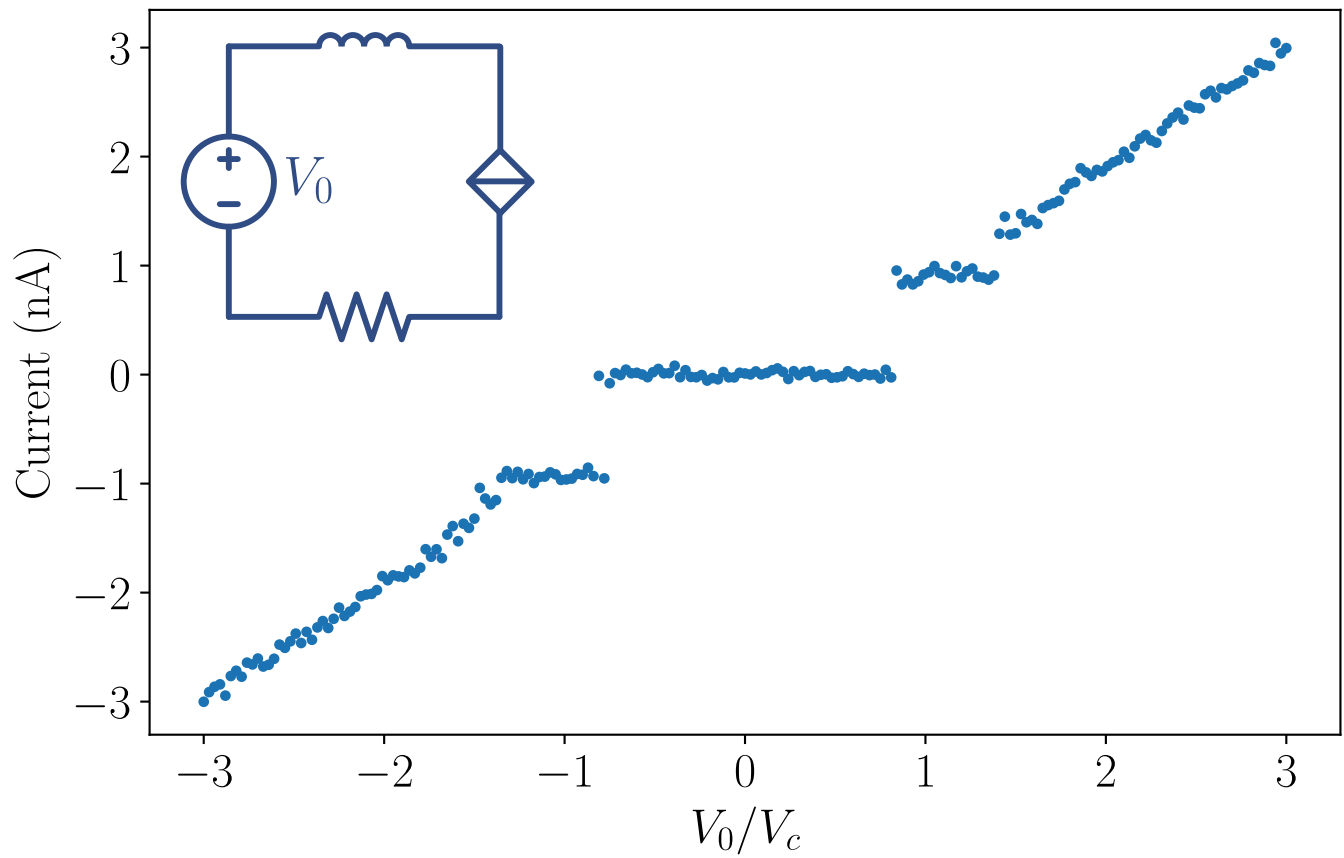
Extended data is available for this paper at <https://doi.org/10.1038/s41567-023-01961-4>.

Supplementary information The online version contains supplementary material available at <https://doi.org/10.1038/s41567-023-01961-4>.

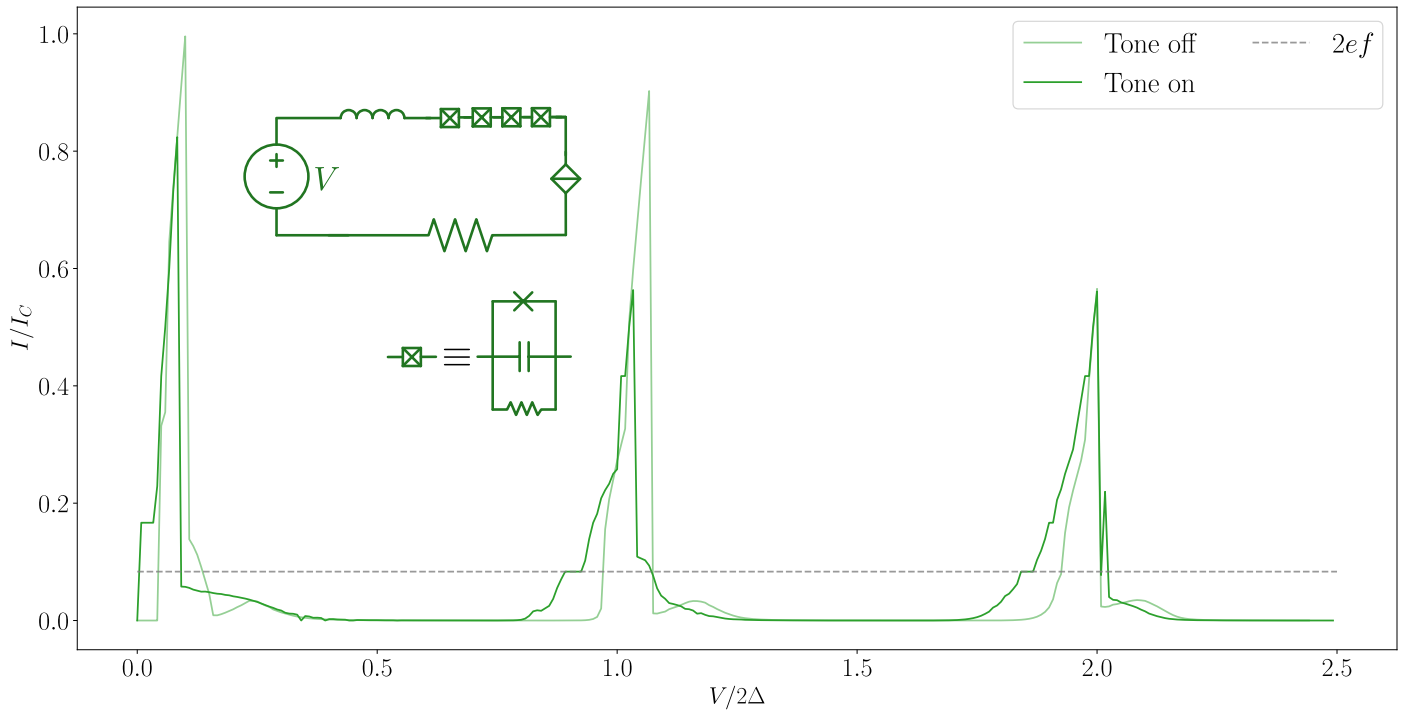
Correspondence and requests for materials should be addressed to Nicolas Roch.

Peer review information *Nature Physics* thanks Samuel Benz and the other, anonymous, reviewer(s) for their contribution to the peer review of this work.

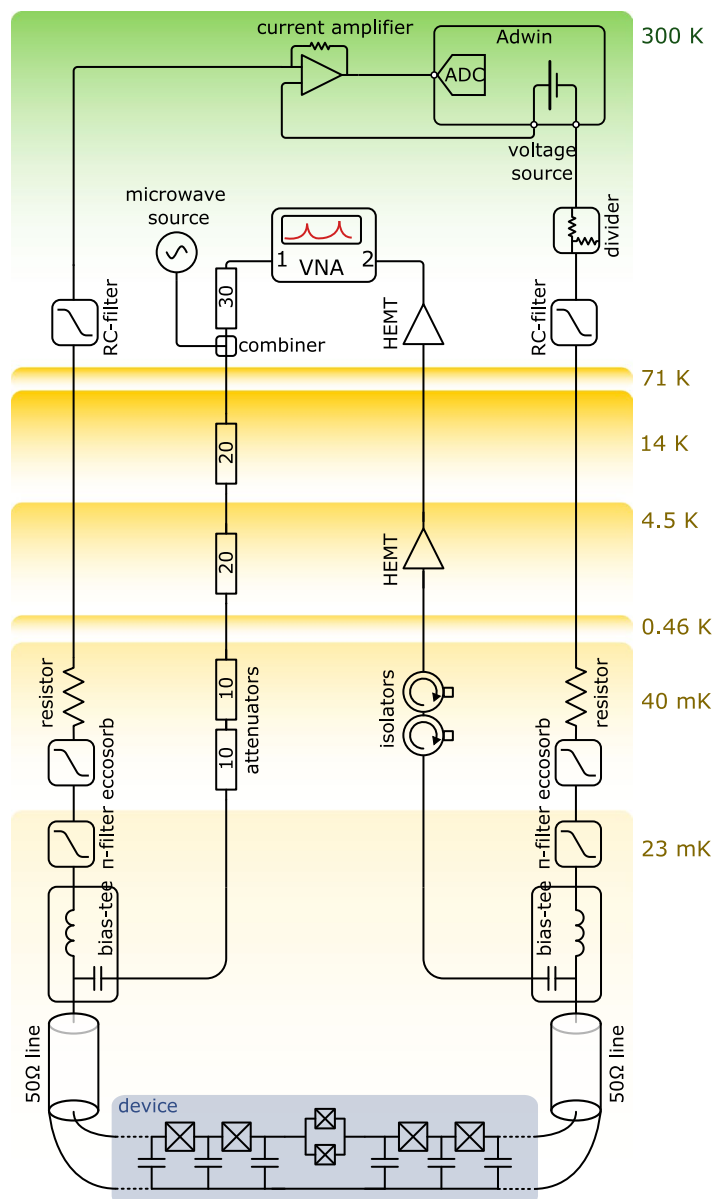
Reprints and permissions information is available at www.nature.com/reprints.



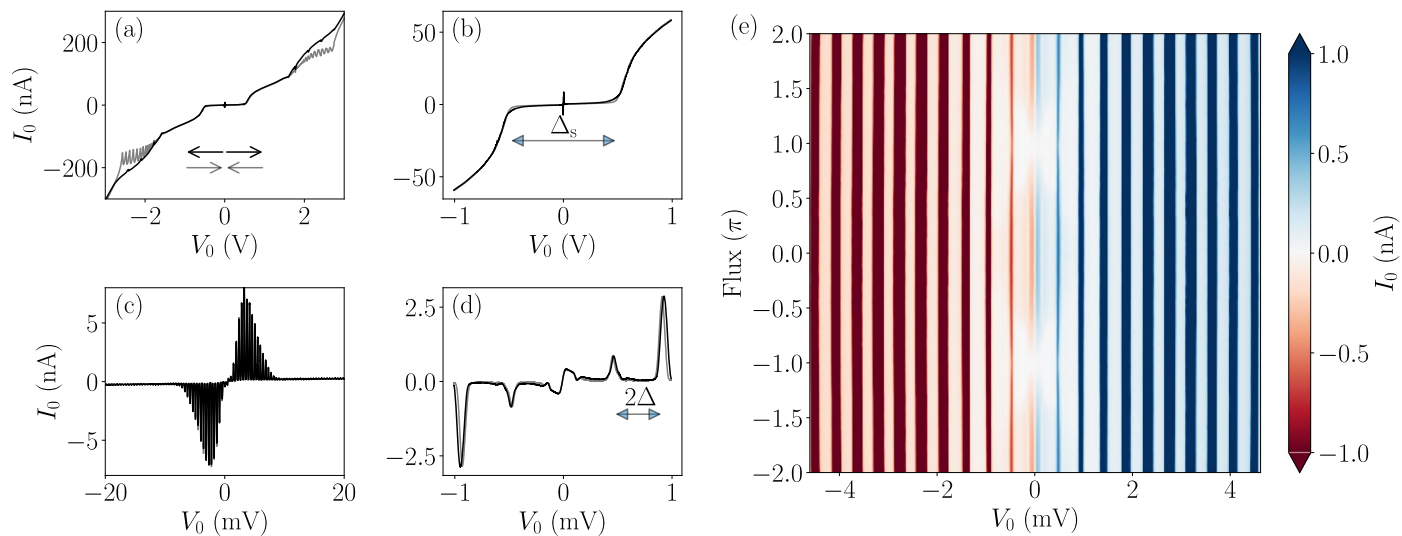
Extended Data Fig. 1 | Simulation of the CJLR circuit under microwave irradiation with experimental noise. These IV curves are used to determine how clear are the steps for different parameter combinations and do not resemble the actual steps observed in our device. The inset is the simulated circuit, where the diamond is the non-linear capacitor ($\cos(\frac{\pi}{2}Q)$ element).



Extended Data Fig. 2 | Simulated IV curve of a chain of four junctions in series with an inductance, a resistor, and a non-linear capacitor with and without an AC drive of frequency f . Current plateaux of height $2ef$ are observed before each 2Δ current peak in qualitative agreement with the experimental observations.

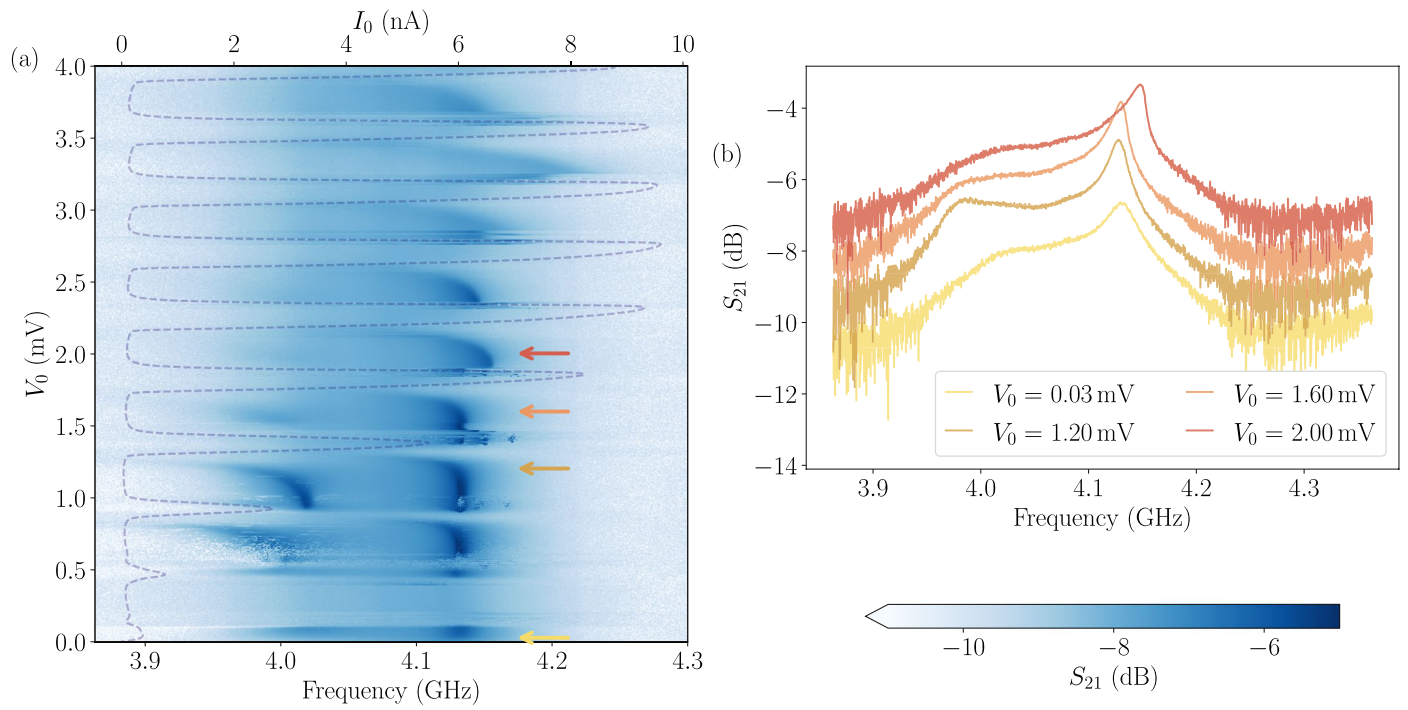


Extended Data Fig. 3 | Experimental setup used in this work. The yellow boxes show the different stages of the dilution refrigerator with their temperatures on the right side, while the part of the apparatus at room temperature is in green. The device is in grey at the bottom of the figure, the reader is referred to the main text for its description.

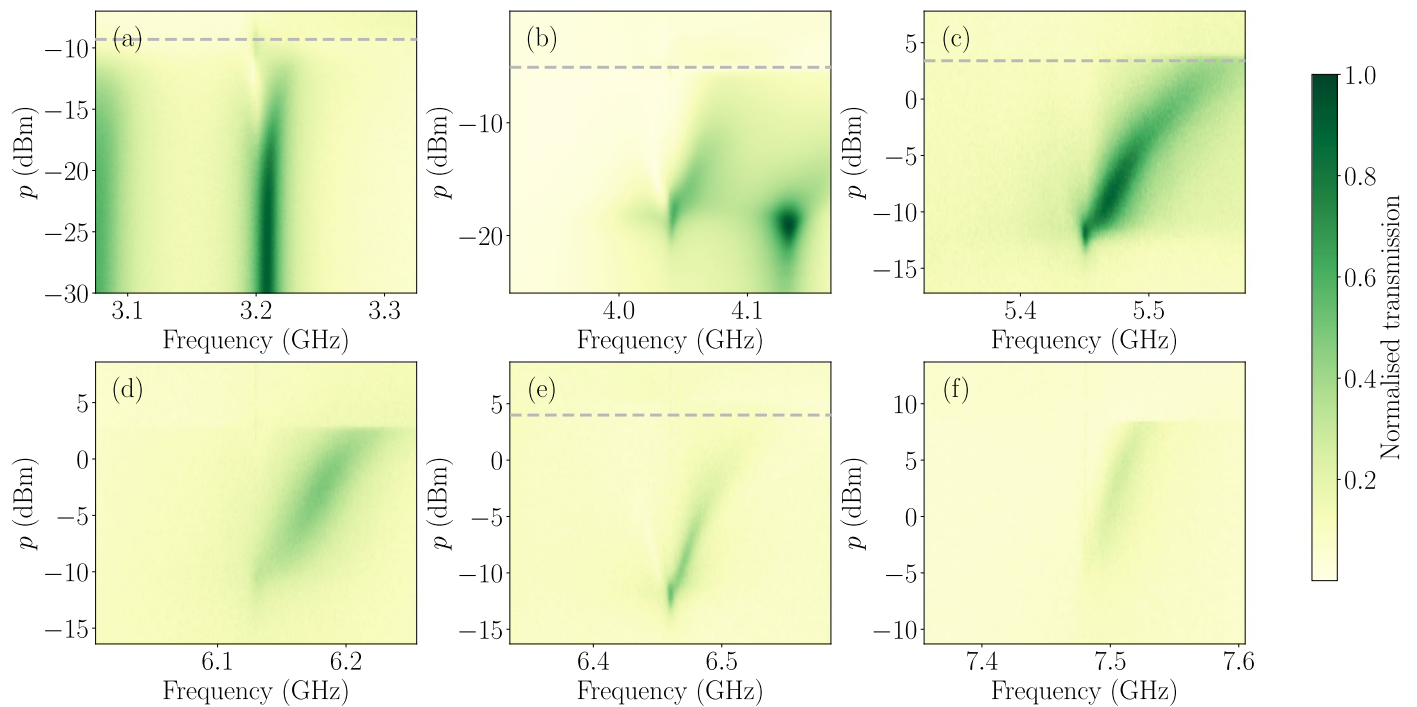


Extended Data Fig. 4 | Full IV curve of the Bloch array. Plots (a) to (d) show the IV curve at different scales, and the black (grey) line indicates increasing (decreasing) $|V_0|$, as shown by the arrows in (a). The voltage scale is gradually

reduced from (a) to (d); discrepancies between the current amplitude in the plots are related to measurement conditions. Finally, (e) shows the flux dependence of the Bloch array's IV characteristic at low voltages.



Extended Data Fig. 5 | Combined microwave and DC measurements. Plot (a) is the variation of the transmission with respect to V_0 , where the IV was superimposed to the plot as a dashed line for illustrative purposes. In (b) we show slices of (a) at different voltages, where a 1 dB offset for each curve is added for clarity.



Extended Data Fig. 6 | Power dependence of the microwave transmission of the odd modes of the Bloch array. Power sweep of the odd modes identified in the Bloch array, ranging from (a) at 3.2 GHz to (f) at 7.5 GHz. For each plot we observe the same power-dependent behavior, analogue to the one of Fig. 4b

(see the main text for more details). These measurements are used to find the correct power to obtain the locking, and thus the steps. Such power is signaled with a dashed grey line for the modes where it could be identified, and the resulting current plateaux are shown in Fig. 5c.